

Cosmic-CoNN: A Cosmic Ray Detection Deep-Learning Framework, Dataset, and Toolkit

CHENGYUAN XU (许程远),^{1,2} CURTIS McCULLY,³ BONING DONG (董泊宁),⁴ D. ANDREW HOWELL,^{3,5} AND PRADEEP SEN⁴

¹ *Media Arts and Technology, University of California, Santa Barbara, CA 93106, USA*

² *Department of Computer Science, University of California, Santa Barbara, CA 93106, USA*

³ *Las Cumbres Observatory, 6740 Cortona Drive, Suite 102, Goleta, CA 93117-5575, USA*

⁴ *Department of Electrical and Computer Engineering, University of California, Santa Barbara, CA 93106, USA*

⁵ *Department of Physics, University of California, Santa Barbara, CA 93106, USA*

ABSTRACT

Rejecting cosmic rays (CRs) is essential for scientific interpretation of CCD-captured data, but detecting CRs in single-exposure images has remained challenging. Conventional CR-detection algorithms require tuning multiple parameters experimentally, making it hard to automate across different instruments or observation requests. Recent work using deep learning to train CR-detection models has demonstrated promising results. However, instrument-specific models suffer from performance loss on images from ground-based facilities not included in the training data. In this work, we present **Cosmic-CoNN**, a deep-learning framework designed to produce generic CR-detection models. We build a large, diverse ground-based CR dataset leveraging thousands of images from the *Las Cumbres Observatory* global telescope network to produce a generic CR-detection model which achieves a 99.91% true-positive detection rate and maintains over 96.40% true-positive rates on unseen data from *Gemini GMOS-N/S*, with a false-positive rate of 0.01%. Apart from the open-source framework and dataset, we also build a suite of tools including console commands, a web-based application, and Python APIs to make automatic, robust CR detection widely accessible by the community of astronomers.

Keywords: Astronomy data reduction, CCD observation, Cosmic rays, Neural networks, Classification

1. INTRODUCTION

Cosmic rays (CRs) are a key source of artifacts in data from astronomical observations using charge-coupled devices (CCDs). These charged particles excite electrons in the detector, creating artifacts that can be mistaken for astronomical sources. Space-based instruments like the *Hubble Space Telescope (HST)*, which are not protected by Earth's atmosphere, are heavily affected by CR, with an average flux density of 0.96 CR/s/cm² (Miles et al. 2020). Ground-based instruments are also affected but at a rate about four orders of magnitude lower, typically of ~ 0.00001 CR/s/cm² in thin CCDs, as observed in *Las Cumbres Observatory* global telescope network imaging data. CCD thickness is another factor that affects an imager's sensitivity to CRs.

Corresponding author: Chengyuan Xu
 cxu@ucsb.edu

Detecting CRs is straightforward when multiple exposures of the same field are available (see example in Fig. 1). By comparing the deviation of a pixel from the mean or median value in a stack of aligned images, CRs (and other artifacts) can be effectively identified (Windhorst et al. 1994; Zhang 1995; Freudling 1995; Fruchter & Hook 2002; Desai et al. 2016). However, multiple exposures may not be available, especially for spectroscopic observations. Variations in image quality (e.g., seeing) can also complicate this procedure, so robust detection of CR pixels on individual images is still necessary.

CRs do not travel through the telescope's optical path nor do they follow the point spread function (PSF): they are not blurred by the atmosphere and are therefore sharper than a real PSF. Furthermore, they can come in any incidence angle to have less symmetrical morphologies than real astronomical sources. Several algorithms leverage this feature, like adapted PSF convolution (Rhoads 2000), histogram analysis (Pych 2004),

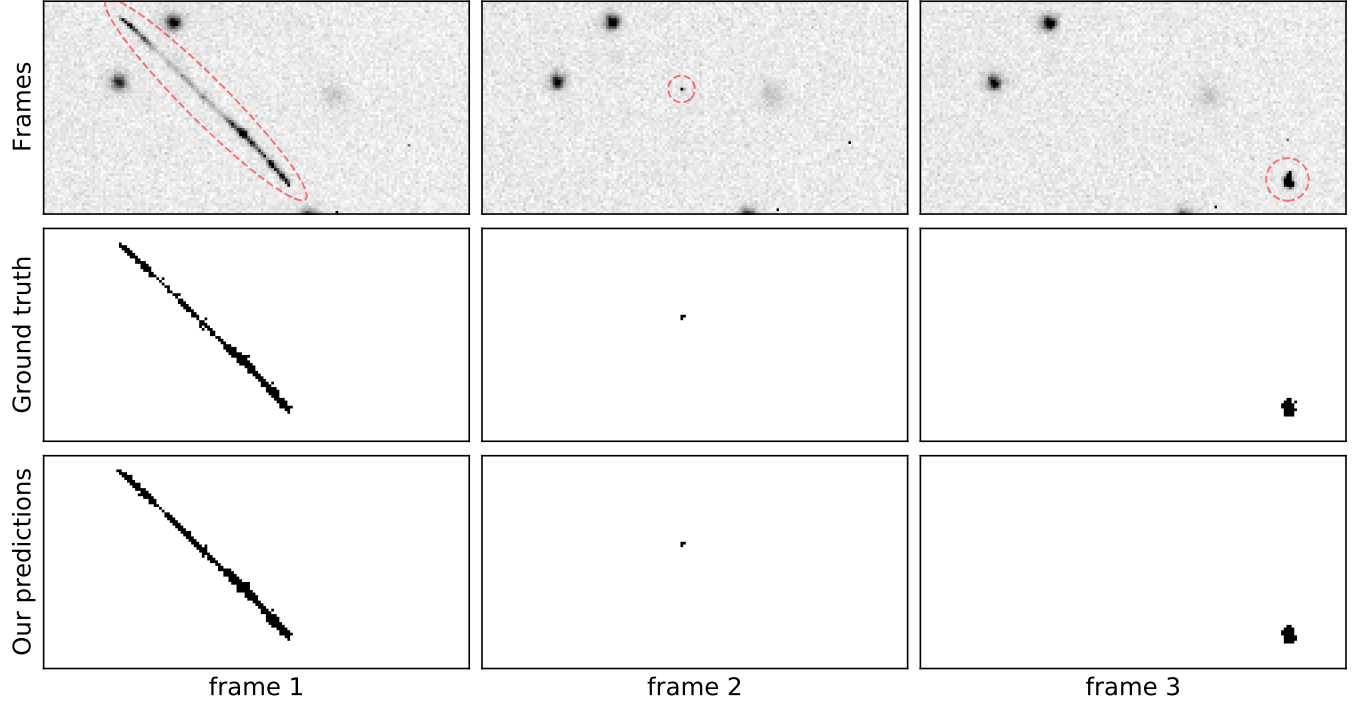


Figure 1. Cosmic rays (CRs), labeled with red circles, and other artifacts can be identified by comparing a pixel’s deviation from the pixel location’s median value in a stack of aligned exposures taken minutes apart. Our deep-learning model predicts a probability map P where $P_{ij} \in [0, 1]$ indicating the likelihood of a pixel being affected by CR using a single frame.

fuzzy logic-based algorithms (Shamir 2005), and Laplacian edge detection (van Dokkum 2001). These methods and the IRAF task like `xzap` by M. Dickinson often require adjusting one or more hyper-parameters experimentally to obtain the best result per image. Machine learning algorithms like k-nearest neighbors, multilayer perceptrons (Murtagh & Adorf 1991), and decision-tree classifiers (Salzberg et al. 1995) showed promising results on small HST datasets, but lacked generality when compared to image-filtering techniques like `LA Cosmic` (van Dokkum 2001).

Machine-learning methods have been widely adopted in astronomical research recently (see Baron (2019) for a review). Zhang & Bloom (2020) used a convolutional neural network (CNN) to identify CR contaminated pixels in *Hubble Space Telescope (HST) ACS/WFC* images, in a method called `deepCR`. In contrast to using the Laplacian kernel (Chen et al. 1987) for edge detection as is in `LA Cosmic`, the convolution kernels in `deepCR` learn the intrinsic characteristics of the CR artifacts, enabling it to detect CRs of arbitrary shapes and sizes.

The `deepCR` model outperforms the state-of-the-art method `LA Cosmic` without manual parameter tuning, demonstrating the promise of deep learning for CR detection. The neural network architecture of `deepCR`, however, makes it sensitive to differences in CR rates

and morphologies limiting its applicability to other instruments, specifically ground-based data with variable conditions from multiple instruments. Furthermore, the low CR rates in ground-based data makes it more difficult to train a CNN-based model. The $\sim 1:10,000$ ratio between CR and non-CR pixels in our ground-based training data leads to the class-imbalance issue (Buda et al. 2018) that provides too few CR pixels for spatial convolution, rendering the learning very inefficient.

To address these issues, we present `Cosmic-CoNN`, a deep-learning framework designed to train generic CR detection models for ground-based instruments by explicitly addressing the class-imbalance issue and optimizing the neural network for the astronomical images’ unique spatial and numerical features. `Cosmic-CoNN` also generalizes to other types of data like space-based and spectroscopic observations.

We leverage the publicly available data from *Las Cumbres Observatory (LCO)* to build a large, diverse CR dataset. *LCO*’s `BANZAI` data pipeline (McCully et al. 2018) ensures data from different telescopes is not dominated by instrumental signature artifacts. It allows us to label CRs consistently in thousands of observations taken across a wide variety of sites with diverse scientific goals. The LCO CR dataset promises the rich feature

coverage required for a generic CR detection model that would work for a variety of ground-based instruments.

This paper is organized as follows: we present the LCO CR dataset in §2 and discuss the deep-learning CR-detection framework in §3. Extensive evaluations on various types of observations are presented in §4. We introduce the toolkit and the software APIs in §5, and conclude the paper with a discussion in §6.

2. LCO CR DATASET

Deep-learning models are data driven. A robust and generic CR-detection model requires a large number of diverse observations from various instruments and the CRs need to be labeled accurately and consistently across different instruments. With this in mind, we build a custom `Python` CR-labeling pipeline to generate a large cosmic ray ground-truth dataset, leveraging some unique characteristics of *Las Cumbres Observatory (LCO)* global telescope network.

Our CR-labeling pipeline stacks consecutive images of the same field with the same filter to identify cosmic rays. To limit artifacts due to variations in CCD response, we only selected sequences that have at least three repeated observations with the same exposure time. The LCO CR dataset consists of over 4,500 scientific images from *LCO*'s 23 globally distributed telescopes. About half of the images are $4K \times 4K$ pixels resolution and the rest are $3K \times 2K$ or $2K \times 2K$. To the best of our knowledge, this is the largest dataset of its kind. Each sample in our dataset is a multi-extension `FITS` file including three images, three corresponding CR masks, and three ignore masks. The implementation of our ground-truth CR-labeling pipeline is presented in Appendix A.

A variety of CCD imagers with different pixel scales, field of views, and filters were used in each telescope class of *LCO*'s global telescopes network (Table 1). From a deep-learning perspective, diverse data greatly benefits model generality. But having ground-truth CRs labeled consistently on different instruments is not a trivial task. The `BANZAI` data reduction pipeline (McCully et al. 2018) performed instrumental signature removal (bad-pixel masking, bias and dark removal, flat-field correction), making *LCO* data suitable for building such a dataset. Instrument artifacts exist as two identical CCDs could have different response curves after years of bombardment by photons and cosmic rays. The standardized data reduction is key to allow our CR-labeling pipeline to consistently and accurately label CRs across various instruments.

We chose images from across three telescope classes and across the year as shown in Fig. 2. Images from

Table 1. LCO science imagers covered in the CR dataset.

Imager	Class	Pixel Scale (Binning)	FOV	Filters
SBIG 6303	0.4 m	0.571 (1×1)	29' × 29'	9
Sinistro	1 m	0.389 (1×1)	26' × 26'	21
Spectral	2 m	0.300 (2×2)	10' × 10'	18

NOTE—Pixel Scale: "pix⁻¹.

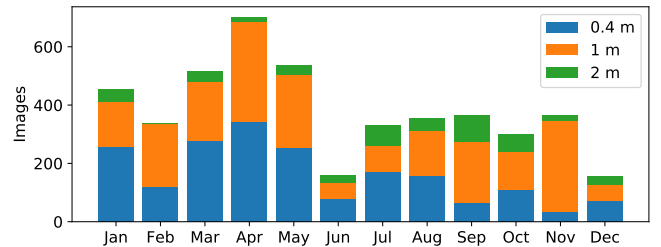


Figure 2. LCO CR dataset sample distribution by month and telescope class, from November 2018 to December 2019. Diverse source densities sampled around the year help improve model robustness.

different times of the year sampled a variety of source densities for different sets of scientific goals. The varying source density proved to be of great importance to robust CR detection (Farage & Pimbblet 2005). In the task of CR detection, diversified real objects provide rich features for the negative class, which greatly improves model robustness.

We further constrained a sequence of exposures to come from the same scheduling unit: the frames are typically separated by just a few minutes. Repeated exposures in a short period of time help mitigate the point spread function (PSF) variation induced by atmospheric attenuation but PSF wings still cause noticeable false positive labels adjacent sources. For our training data we reject CRs that are overlapping with astronomical sources so that variations in the PSF do not create artifacts in the training sample.

Of all CR pixels, 1.21% were rejected in an effort to tackle the PSF-variation-induced artifacts. This trade-off ensures the remaining 98.79% CR pixels are labeled at higher confidence. Therefore, models trained with this dataset focus on distinguishing CRs from real sources, and it is anticipated that CRs overlapped with sources will not be detected. Training on raw images with arbitrary PSFs also guarantees consistent performance at inference time. In future versions we will model the PSF explicitly to make sure that we do not bias our training sample.

Our dataset is not affected by transient sources that evolve at a timescale of hours or longer because of the very tight space between exposures. At this timescale,

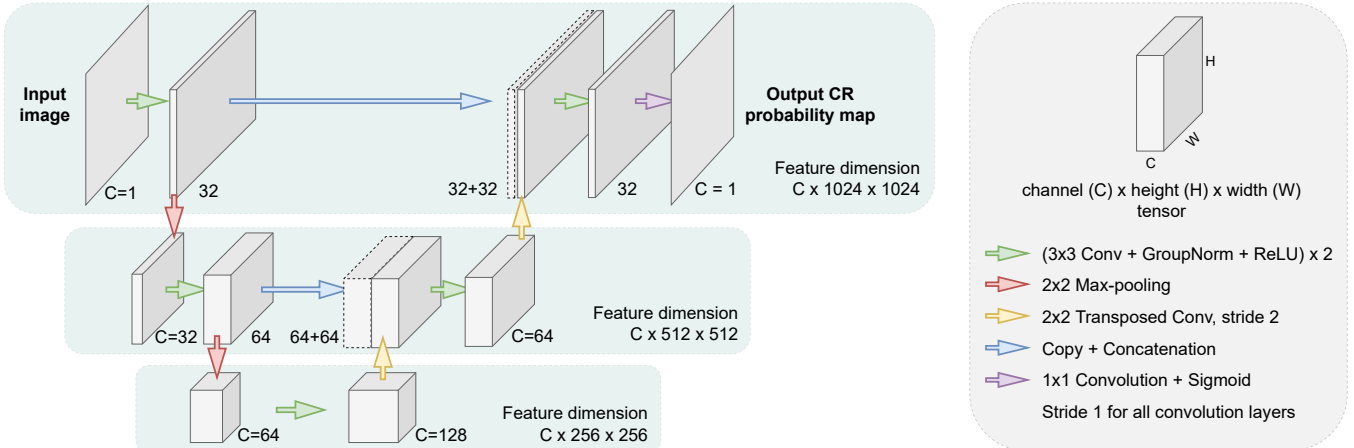


Figure 3. Cosmic-CoNN’s neural network architecture is based on U-Net. The symmetric design concatenates high-resolution features from the downsampling path to the upsampling path via skip connections (blue arrow) to allow more efficient gradient propagation, thus allowing pixel-level predictions for high-resolution images.

near-Earth objects (NEOs), satellites, and airplanes could still cause false-positive labels in the stack-based CR masks. Large satellite or airplane trails are rejected by our CR-labeling pipeline automatically. A very small fraction of false-positive labels from NEOs and satellites exist but we have manually verified every single mask to ensure their impact is negligible.

3. DEEP-LEARNING FRAMEWORK

Our work is inspired by the recent success of `deepCR` (Zhang & Bloom 2020), a U-Net based deep-learning framework that identifies CR-contaminated pixels in *HST ACS/WFC* imaging data. The U-Net (Ronneberger et al. 2015) is a CNN-based deep-learning architecture which takes an image as input and outputs a probability map of the same size (Fig. 3). U-Net convolves the image at multiple scales and concatenates features of the same scale with skip connections, allowing the network to propagate context information to higher resolution layers, thereby producing pixel-level classification predictions on large images.

In contrast to hand-crafted kernels used in conventional methods (e.g., the Laplacian kernel in `LA Cosmic` (van Dokkum 2001)), a deep CNN model optimizes millions of kernel parameters in its hierarchical convolution layers (green arrows in Fig. 3). Both methods extract features via convolution which takes a small region on the image as input, known as the receptive field. Limited by a small receptive field (the area of the 3×3 Laplacian kernel), `LA Cosmic` (van Dokkum 2001) detects a CR by its outermost pixels’ sharpness and moves inward in an iterative fashion, making the detection computationally expensive and inefficient. A deep CNN model, on the other hand, creates a larger receptive field in deeper layers of its hierarchical network to capture not only

CRs’ morphological features (edges, corners, or sharpness) but also the contextual features from peripheral pixels, allowing it to predict CRs of arbitrary shapes and sizes.

The `deepCR` model achieves 75.2%–93.3% true-positive rates at a false-positive rate of 0.05% on different types of *HST ACS/WFC* observations. Even without GPU acceleration, its computation time is comparable to `Astro-SCRAPPY` (McCully et al. 2018), an optimized version of `LA Cosmic` (van Dokkum 2001). It demonstrates the promise of using deep-learning methods, particularly CNN-based model for CR detection. However, training on ground-based images exposes a number of network architecture and data-sampling limitations that `deepCR` adopted from the U-Net (Ronneberger et al. 2015).

First, it is worth noting that U-Net was initially proposed to solve biomedical image segmentation problems (Ronneberger et al. 2015). The higher dynamic range and extreme spatial variations found in astronomical images need to be addressed explicitly in order to optimize the neural network for these special features in astronomical data. In addition, The high CR rates in *HST ACS/WFC* data does not reflect the extreme class-imbalance issue observed in *LCO* imaging data. The low CR rates make it difficult for `deepCR` to train and converge on the ground-based LCO imaging data.

In `deepCR`, Zhang & Bloom (2020) adopted a two-phase training design to address some of these issues. Assuming correct data statistics are learned in the initial phase, the model freezes feature normalization parameters in the second phase in order to converge, which we will discuss in §3.3. This design works when the inference data shares the same statistics with training data,

i.e., an instrument-specific model could be learned. But it works against our goal of a generic CR detection model that works for a wide variety of ground-based instruments with varying data statistics.

Cosmic-CoNN adopted the effective U-shaped architecture and proposed a combination of three improvements working symbiotically to tackle the above issues: (§3.1) a novel loss function that specifically addresses the class-imbalance issue, (§3.2) better data sampling approaches that proved to be vital for training efficiency, and (§3.3) a feature normalization method that improves model generality.

3.1. Median-Weighted Loss Function

The CR-detection task is in essence a pixel-wise binary classification problem. Our goal is to learn a function f which takes an image I as input and outputs P , the probability map of each pixel being affected by CR: $P = f(I)$, $P_{ij} \in [0, 1]$, where ij is the pixel coordinate. The user could then apply an appropriate threshold on P to acquire the binary CR mask.

Binary cross entropy (BCE) is commonly used to optimize classification models, and **deepCR** (Zhang & Bloom 2020) used it to calculate the loss between the prediction P and the ground-truth CR mask Y :

$$\text{BCE}(P, Y) = -(Y_{ij} \log(P_{ij}) + (1 - Y_{ij}) \log(1 - P_{ij})) \quad (1)$$

where the ground-truth mask Y is defined as $Y_{ij} = 1$ for CR pixels and $Y_{ij} = 0$ for non-CR pixels. The first term $Y_{ij} \log(P_{ij})$ measures the loss for CR pixels, while the second term becomes 0 when $Y_{ij} = 1$. The second loss term measures non-CR pixels, when $Y_{ij} = 0$. The optimization objective is to minimize the total loss, which is the sum of the two loss terms to account for both CR and non-CR classes.

The low CR rates in LCO data lead to the class-imbalance issue (Buda et al. 2018) which causes the non-CR loss to dominate the total loss. Training on *LCO* imaging data, we observed that the effective losses from the two terms in Equation 1 have a ratio of $\sim 1:6300$ (averaged over 10 random experiments), with the second term (non-CR loss) dominating the optimization objective. This verifies the class-balance issue. Therefore, we make a hypothesis that the network will rapidly learn an incorrect function which predicts 0 (not CR) for all pixels since this is the quickest path to minimize the total loss. Close observation to the training process proved our hypothesis correct: regardless of the initialization, the model trained with BCE loss predicts ~ 0.0 for all pixels in just a few iterations, i.e., the incorrect function

is learned because loss from the second term dominates the optimization objective.

Furthermore, background pixels are the culprit for an extra layer of imbalance within the non-CR class. From dark background to bright sources, the non-CR class often covers the image's entire dynamic range (see example in Fig. 4a,b). Although both labeled as 0 in Y (Fig. 4c), the lopsided numerical difference between background and sources in fact creates two subclasses within the non-CR class to introduce inconsistency, making the training path even more convoluted. Close observation to the training process proved us right again: followed by learning the aforementioned incorrect functional that predicts ~ 0.0 for all pixels, we observe the model's prediction for both source and CR pixels approaching 1.0 (CR) simultaneously, i.e., as the model revises itself from the first incorrect function, it learns a second incorrect function that tend to predict all bright objects as CRs.

The class imbalance and the numerical imbalance within the non-CR class are clear indications that we should directly focus on learning to distinguish between CRs and sources. It inspired us to create an adaptive per-pixel weighting factor that prioritizes on CR and source pixels by down-weighting the less useful yet dominant loss from background pixels. By avoiding the inefficient and convoluted learning path, the model could then converge to a better minimum.

Since we already worked on a sequence of consecutive exposures while building the LCO CR dataset, we could use the CR-free median frame (Fig. 4b) as an unique ground-truth to separate sources from the background. The brightness variation between different sources makes it hard to use the median frame as a weight mask directly, so we perform a series of transformations (sky subtraction, clipping between one and five robust standard deviations, 5×5 kernel with $\sigma = 2$ Gaussian smoothing, unit normalization, and finally clamping with a lower-bound parameter α) to separate sources from the background to acquire the median-weighted mask (M) shown in Fig. 4d. We apply M to the non-CR loss term in BCE to get the novel Median-Weighted Loss Function (L_M):

$$L_M(P, Y, M) = -(Y_{ij} \log(P_{ij}) + M_{ij}(1 - Y_{ij}) \log(1 - P_{ij})) \quad (2)$$

where $M_{ij} \in [\alpha, 1]$. Pixel by pixel, M adaptively down-weights the loss from background by scaling with the lower bound α , mitigating the extreme imbalance between the two loss terms and redefines the optimization objective to directly learning to distinguish between sources and CRs.

With M applied to the second term in BCE, it immediately reduces the effective CR to non-CR class losses to $\sim 1:300$ in Equation 2, comparing to the $\sim 1:6300$ using Equation 1 (in identical conditions). Although this ratio can be further reduced with a more aggressive weight mask, the median-weighted mask preserves all real sources without introducing inconsistency. After training with 500 images, the effective loss of the two terms further reduce to $\sim 1:6$ using L_M , comparing to $\sim 1:110$ using BCE loss.

The Median-Weighted Loss Function effectively suppresses the dominating loss from background pixels, at the same time prioritizes on learning to distinguish between CRs and sources by maintaining their weighting factor at 1. As training progresses, the lower bound α linearly increases the weight for background pixels from 0 to 1 so the model could learn a clear boundary for CRs. We could also cap α smaller than 1 to learn a model that produces CR prediction with soft edges, leaving more control to the user-defined threshold when a binary CR mask is needed. Instead, we choose to increase α to 1 so that L_M converges to BCE loss because the standard Sigmoid function (Little 1974; Little & Shaw 1978) at the last layer of our network theoretically produces a clear classification boundary around 0.5, helping us to better evaluate the model's performance.

We also experimented using the Dice overlap (Sudre et al. 2017) as the loss function but the model learned a strong bias to avoid CRs near real objects, making the more interpretable BCE-based loss a better choice for optimization. Our novel Median-Weighted Loss Function (L_M) makes use of the median frame's unique CR-free property as a robust weighting factor to guide the model's learning path. L_M converges the model to a better minimum by preventing the model from learning incorrect functions during training, and also improves training efficiency with a better convergence path.

3.2. Data sampling

Stochastic gradient descent (Robbins & Monro 1951) is commonly used to optimize modern large-scale deep-learning models. Motivated by stochastic methods' efficiency benefits, at the same time constrained by the ever-growing dataset size and limited GPU memory (usually on the order of 10 GB) for parallel computation, model parameters are iteratively optimized over a small batch of data, colloquially known as a mini-batch, randomly sampled from the full dataset. If iterating over all N samples in a dataset is considered an *epoch*, then training a model with n samples in a mini-batch means the model updates about $\lfloor \frac{N}{n} \rfloor$ times in an epoch (Bottou et al. 2016).

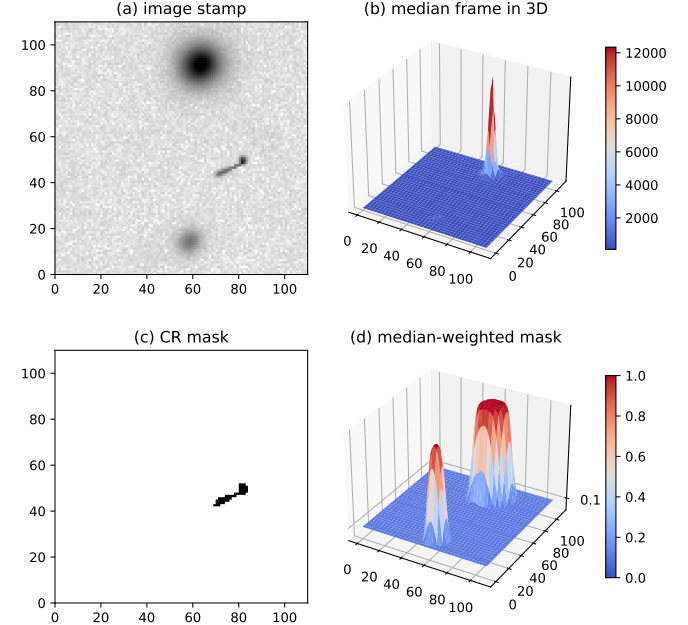


Figure 4. (a) An image stamp that includes sources, CR affected pixels, and background. (b) 3D visualization of the CR-free median frame, representing the non-CR class pixels. The non-CR class is inconsistent because it could be further split into two sub-classes: sources and background. However, the brightness variation between sources makes it hard to separate sources from the background. (c) The ground-truth CR mask. We transform (b) to acquire (d), the median-weighted mask (M) to adaptively down-weight background pixels in the Median-Weighted Loss Function. $M_{ij} \in [\alpha, 1]$, $\alpha = 0.1$ in this figure.

Having the entire *HST ACS/WFC* dataset sliced and stored in 256^2 pixels image stamps, Zhang & Bloom (2020) adopted the U-Net's data-sampling approach that randomly draws $n \times 256^2$ image samples as a mini-batch (Ronneberger et al. 2015). This widely adopted sampling approach is unsuitable for ground-based astronomical images: a small 256^2 stamp might not include a single CR making the stamp not useful for training.

Recall that each sample in the LCO CR dataset is a multi-extension FITS including a sequence of three images between $2K \times 2K$ and $4K \times 4K$ pixels. This design empowers a more flexible data-sampling strategy than having the dataset stored in a fixed size. The **Cosmic-CoNN** framework could crop a stamp of any size up to the entire image from each FITS, ensuring a decent count of CRs in every mini-batch. By sampling only one stamp from each FITS sequence, we also avoided similar observation and improved data representation in a mini-batch. The sparsity of source and CR in ground-based astronomical data motivated us to increase the sampling stamp size to 1024^2 pixels. A larger area is more likely

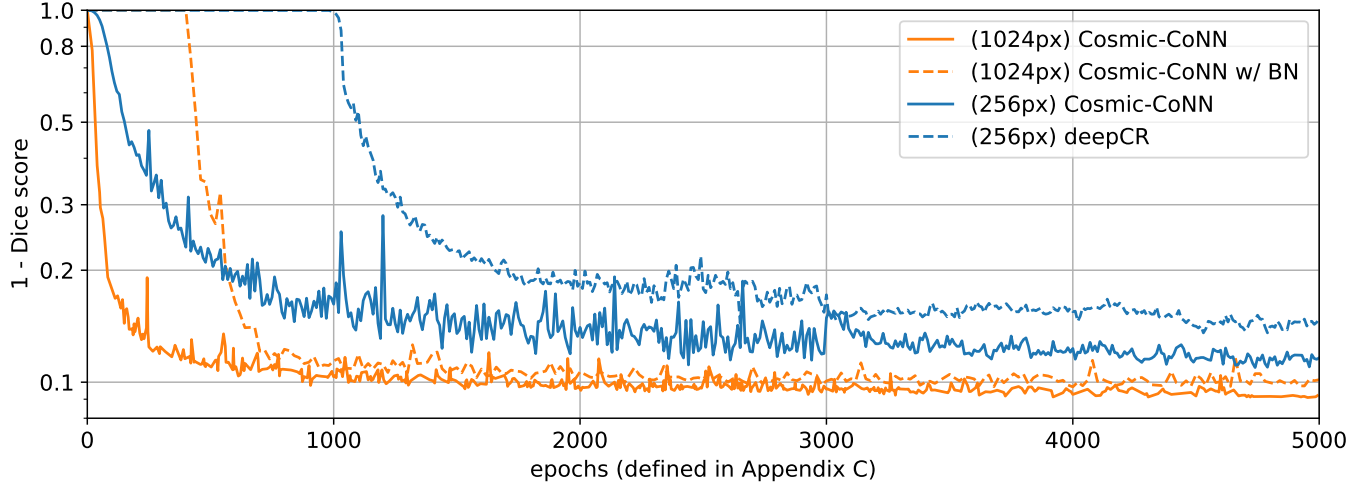


Figure 5. Model performance as a function of training progress. Performance is measured by the Sørensen-Dice coefficient (Sørensen 1948) (henceforth, the Dice score) to gauge the similarity between the model’s prediction and the ground-truth CR mask. Here we use $(1 - \text{Dice score})$ to plot in logarithmic scale, lower is better. Details of the training settings can be found in Appendix C. By avoiding learning incorrect functions at the beginning of the training (discussed in §3.1), Cosmic-CoNN converges rapidly and continues to improve while variant models using batch normalization (BN) or smaller sampling stamp size (256px) not only have less optimal performance on LCO data but also worse generality (see ablation study in Appendix B). deepCR and the Cosmic-CoNN BN variant both train in two different phases. The initial phase (first 400 epochs) learns the scaling and shifting normalization parameters (§3.3), Cosmic-CoNN BN starts to converge immediately after freezing the learned parameters in the second phase, while deepCR does not improve until over 1000 epochs.

to include all three types of features: sources, CRs, and background in a single stamp.

We conducted extensive experiments and proved that CR-detection models optimize more effectively on larger stamps than on many small stamps. In Fig. 5 (solid orange vs. solid blue), we compare two models’ training progress with stamp size being the only difference. Let n be the number of samples in a mini-batch. We used $n = 10$ for the 1024^2 stamps and $n = 160$ for the 256^2 stamps to ensure the models were seeing the same number of pixels in a mini-batch. Models trained on larger stamps always converge to a better minimum, in less iterations, and less wall-clock time.

Finally, in addition to randomly cropping image stamps with increased size, we perform weak data augmentation like random rotation as well as horizontal and vertical flipping, allowing the model to learn invariance to pose variation in astronomical observations. Strong augmentations like elastic deformations adopted by Ronneberger et al. (2015) have proved to be effective to improve performance on a small dataset but we avoided such deformation as it could change real CRs’ sharper profiles. Given the large number of diverse samples in LCO CR dataset, we found weak augmentations sufficient for our dataset. With pose augmentation, we also saw more stabilized training and improved perfor-

mance on *HST ACS/WFC* data, showing that weak augmentation is effective in increasing model robustness.

3.3. Group normalization

Feature-normalization techniques accelerate training and make deep neural networks more amenable to optimize. Batch normalization (BN) (Ioffe & Szegedy 2015) is an important feature-normalization method widely used in deep CNN architectures for various tasks, including in deepCR (Zhang & Bloom 2020). As its name suggests, BN calculates the mean μ_i and variance σ_i^2 over a mini-batch of data x_i and learns two parameters γ and β to scale and shift the inputs x_i for feature normalization:

$$\hat{x}_i = \gamma \frac{x_i - \mu_i}{\sqrt{\sigma_i^2 + \epsilon}} + \beta. \quad (3)$$

When the training completes, a pair of global γ and β parameters suitable for the training data are stored in every normalization layer, and they are also used at inference time for new data. But memorizing constant normalization parameters in the model could introduce a discrepancy between BN’s training and inference behavior when the inference data does not share consistent statistics with training data (Summers & Dinneen 2019).

In the context of CR detection, this feature of BN becomes a strong limitation to learn a generic model. The varying statistics in data from a variety of ground-based instruments means a model trained for one instrument

will not generalize well to another because each CCD imager will need unique γ and β parameters in a new model that is trained separately. We were able to verify this intuition as we observed a larger performance loss from BN-based models than models without BN when testing new data from unseen instruments (see Sec. 4.2).

Furthermore, the high dynamic range and high variance in astronomical imaging data make it difficult to learn accurate γ and β from the stochastic sampling. This behavior is mitigated by `deepCR`'s two-phase training as the model freezes the γ and β in the second phase, assuming correct parameters are learned in the first phase. As shown in Fig. 5, the two models using BN (dashed curves) both suffer from delayed and less optimal convergence. Thus we need a normalization method that does not rely on learning data-dependent scaling and shifting parameters to optimize model generality.

Group normalization (GN) introduced by Wu & He (2018) is a feature normalization technique that is independent of constant normalization parameters. GN divides the feature channels into groups and computes the mean and variance within each group for normalization. The insight is to force the network to learn abstract internal structures to adapt to the diverse input instead of saving constant parameters.

By freeing the model from fixed scaling and shifting parameters, the `Cosmic-CoNN` model using GN has a more consistent performance when tested on data from unseen instruments (see performance loss in Table 2). GN is also effective at optimizing training efficiency on both ground- and space-based astronomical data. As shown in Fig. 5, the `Cosmic-CoNN` model (solid orange) outperforms its BN variant model (dashed orange) in both convergence speed and accuracy.

In addition, the increased stamp size proposed in §3.2 will force the same amount of GPU memory to fit less images in a mini-batch. Increasing the stamp width and height by m times will reduce the batch size n to $\frac{n}{m^2}$. The accuracy of batch normalization decreases rapidly when the batch size becomes too small, so adopting the proposed larger stamp size alone might even hurt model accuracy. The group normalization, on the other hand, is independent of the batch size, allowing group normalization to work symbiotically with the larger stamp size to improve `Cosmic-CoNN`'s performance.

As a common practice in deep-learning research, in Appendix B we demonstrate the effectiveness of L_M , larger stamp size, and group normalization through ablation study, a series of controlled experiments that each replaces a single building block in a machine learning system to better understand its causality to the overall performance.

4. RESULTS

We trained and evaluated the `Cosmic-CoNN` framework on three types of data: ground-based imaging, space-based imaging, and ground-based spectroscopic observations to demonstrate the framework's broad applicability. For ground-based imaging data, we trained both `Cosmic-CoNN` and `deepCR` (Zhang & Bloom 2020) models on LCO CR dataset with identical settings (§4.1). We also evaluated the test data with the filtering-based CR detector `Astro-SCRAPPY` (McCullly et al. 2018). Models trained on *LCO* data are further tested on images from *Gemini Observatory's GMOS North and South* telescopes (Gillett et al. 1996) to understand how well the models generalize to unseen data from other ground-based instruments (§4.2). For space-based imaging data, we trained the `Cosmic-CoNN` model on the *HST ACS/WFC* dataset that Zhang & Bloom (2020) released and compared with the official released `deepCR` CR detection model (§4.3). Finally, we trained a `Cosmic-CoNN` spectroscopic model using *LCO* data and saw exceptional performance (§4.4). Details of the training environment and experiment settings are presented in Appendix C.

We use receiver operating characteristic (ROC) curves as an evaluation metric to compare different detectors' performance at varying thresholds. An ROC curve depicts relative tradeoffs between benefits (true-positive rate, TPR) and costs (false-positive rate, FPR) (Fawcett 2006). In the context of CR detection:

$$\text{TPR} = \frac{\text{CR pixels correctly found}}{\text{All CR pixels}}, \quad (4)$$

$$\text{FPR} = \frac{\text{Non-CR pixels mistaken as CR}}{\text{All non-CR pixels}}. \quad (5)$$

Simply put, a higher TPR is desirable at a fixed FPR. While ROC provides a model-wide evaluation at all possible thresholds, standard ROC can be misleading for imbalanced datasets which have many fewer CR pixels than non-CR pixels. As shown in Table 2, there is a visible performance gap between *LCO* and *HST* imaging data at the FPR of 0.01%, which is caused by the drastically higher CR rates in space-based data making it a more challenging task. It requires special caution to interpret TPR at fixed FPR on imbalanced data.

The Precision-Recall curve, on the other hand, is a more robust metric for imbalanced datasets (Saito & Rehmsmeier 2015). While recall is equivalent to TPR, in the context of CR detection, precision is defined as:

$$\text{Precision} = \frac{\text{CR pixels correctly found}}{\text{All CR pixels predicted by model}}. \quad (6)$$

Unlike FPR, precision is determined by the proportion of correct CR predictions given by the model, which is

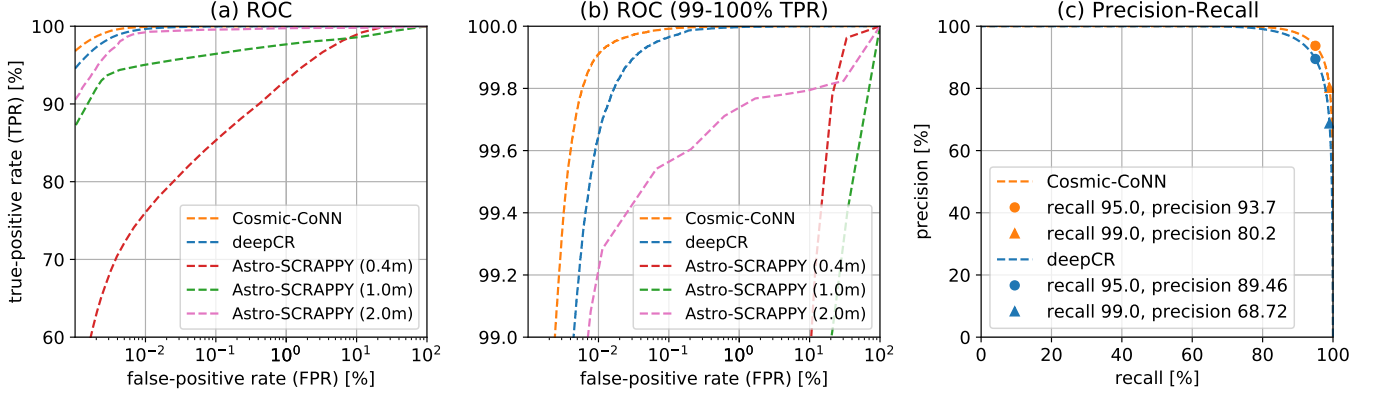


Figure 6. Evaluating various CR detectors with ROC and Precision-Recall curves on *LCO* imaging data. It is desirable to have a higher true-positive rate (TPR) at fixed false-positive rates (FPR) in ROC (Equation 4,5). As illustrated in (a) and (b), Cosmic-CoNN outperforms other methods with higher TPRs overall. The margin of its lead over other methods further increases in more strict low FPRs, showing Cosmic-CoNN’s robust performance. Markers on the Precision-Recall curves in (c) show when 95% of the CR pixels are found (recall), Cosmic-CoNN’s prediction is over 4% more accurate than deepCR (precision). At 99% recall, Cosmic-CoNN’s lead increases to $\sim 11\%$.

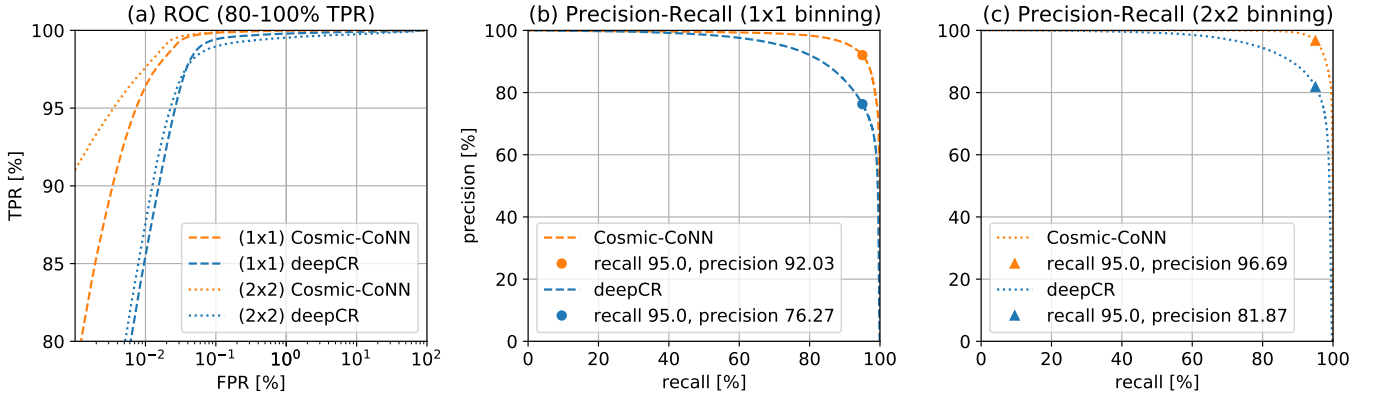


Figure 7. Evaluating *LCO* data trained models on unseen data from *Gemini GMOS-N/S*. ROC curves in (a) and Precision-Recall curves in (b,c) show Cosmic-CoNN has double-digit lead over deepCR in TPR and precision on both *GMOS-N/S* 1×1 and 2×2 binning observations. The consistent performance of Cosmic-CoNN shows our ground-based imaging model is a robust and more generic CR detector for unseen instruments.

less sensitive to the ratio between CR and non-CR pixels in an image, i.e., it is also less sensitive to the varying CR rates between different datasets. Given a fixed proportion of real CRs correctly discovered (e.g., 95% recall), the better model should make less mistakes, thus a higher precision. It also helps us to understand how well a model performs on two different datasets given the same recall, or vice versa.

The Precision-Recall curve can also be used as an indicator of prediction confidence. We used this property to provide supplementary evidence that helped [Hiramatsu et al. \(2020\)](#) determine a candidate progenitor to be a new type of stellar explosion – an electron-capture supernova. We rule out the presence of cosmic-ray hits at or around the progenitor site to determine the peak pixel is an actual stellar PSF with $> 3\sigma$ confidence by plotting

deepCR’s ([Zhang & Bloom 2020](#)) predicted score on the corresponding Precision-Recall curve to read the model precision at the progenitor site.

4.1. *LCO* imaging data

For ground-based imaging data, we randomly sampled and withheld $\sim 10\%$ of images from the LCO CR dataset as the test dataset. We first analyzed the testset using the filtering-based CR detector **Astro-SCRAPPY** ([McCully et al. 2018](#)) for reference. We used `objlim=2.0` for *LCO* 1.0- and 2.0-meter telescopes’ data and `objlim=0.5` for 0.4-meter for optimal performance in different telescope classes. `sigfrac=0.1` is held constant for all telescope classes and we produce the ROC curves by varying the `sigclip` between [1, 20]. The two deep learning methods **deepCR** and **Cosmic-CoNN** are plotted by varying the threshold t .

Table 2. Quantitative results of CR detectors’ performance on various datasets. The true-positive rate (TPR) is evaluated at fixed false-positive rates (FPR) of 0.01% and 0.1%. Ground-based imaging models are trained on *LCO* data and tested on unseen data from *Gemini* telescopes to demonstrate model generality through their relative loss in performance (indicated in brackets). **Cosmic-CoNN** suffers little or no performance loss on *Gemini* data proving it to be a more generic CR detector than the **deepCR** model (Zhang & Bloom 2020). The *HST ACS/WFC* and *LCO* spectroscopic models are trained on corresponding datasets showing the **Cosmic-CoNN** framework is well generalized to other types of data with high performance.

Data	Method	TPR at 0.01% FPR	TPR at 0.1% FPR	Precision at 95% Recall
		(Loss in performance)	(Loss in performance)	
LCO Imaging Data	Astro-SCRAPPY (0m4)	76.04%	85.17%	–
	Astro-SCRAPPY (1m0)	95.03%	96.41%	–
	Astro-SCRAPPY (2m0)	99.21%	99.56%	–
	deepCR	99.65%	99.97%	89.46%
	Cosmic-CoNN	99.91%	99.99%	93.70%
Gemini GMOS-N/S (1×1 binning)	deepCR	85.49% (-14%)	99.43%	76.27% (-13%)
	Cosmic-CoNN	96.40% (-4%)	99.83%	92.03% (-2%)
Gemini GMOS-S (2×2 binning)	deepCR	87.58% (-12%)	98.97%	81.87% (-8%)
	Cosmic-CoNN	97.60% (-2%)	99.88%	96.69% (+3%)
HST ACS/WFC (extragalactic field)	deepCR	80.07%	92.80%	82.22%
	Cosmic-CoNN	80.62%	93.43%	85.11%
HST ACS/WFC (globular cluster)	deepCR	83.44%	95.55%	82.20%
	Cosmic-CoNN	85.51%	96.51%	86.75%
HST ACS/WFC (resolved galaxy)	deepCR	53.34%	73.76%	66.31%
	Cosmic-CoNN	61.97%	80.31%	69.08%
LCO Spectroscopic Data	Cosmic-CoNN	97.40%	99.86%	94.4%

The **Cosmic-CoNN** model achieves 99.91% TPR at a fixed FPR of 0.01%, outperforming other methods, as illustrated in Fig. 6a,b. Quantitative results are presented in Table 2. For both deep-learning models to discover 95% of the real CR pixels (95% recall), the CR predictions given by **Cosmic-CoNN** is over 4% more accurate than **deepCR** (93.70% vs. 89.46% in precision). If we continue to lower the threshold to allow 99% of the CR pixels being found, **Cosmic-CoNN**’s lead increases to ∼11%, as shown Fig. 6c.

Cosmic-CoNN’s lead seems modest in number but is more obvious when visualized. We analyze the detection discrepancy between different methods and present a few typical examples in Fig. 8. Binary masks are acquired using the most suitable threshold for each model. We find that **Cosmic-CoNN** detects CRs more completely, especially the peripheral pixels that other methods tend to miss. The high-fidelity predictions allow **Cosmic-CoNN** to achieve higher accuracy.

4.2. Unseen ground-based data

The goal of this work is to produce a generic ground-based CR detection model. In order to understand how well the models trained on LCO CR dataset perform on unseen instruments, we produced a test dataset consisting of 98 images from the *Gemini Observatory’s GMOS*

North and South telescopes (Gillett et al. 1996). The ground-truth CR masks are reduced by the DRAGONS software (Labrie et al. 2019) with *hsigma*=5.0 to match the setting we used to produce the LCO training data.

The two deep-learning models trained on *LCO* data are tested on unseen data from *GMOS-N/S* telescopes to compare their relative loss in performance, presented in Fig. 7 and Table 2. **Cosmic-CoNN** has consistent or better precision at 95% recall while **deepCR** has −13% and −8% loss in precision on 1×1 and 2×2 binning images, respectively. The lower relative performance loss of about −4% and −2% in TPR at 0.01% FPR (compared to a performance loss of about −14% and −12%, respectively, for **deepCR**), also shows that the **Cosmic-CoNN** framework is superior in producing more generic CR detection models.

Examples of detection discrepancy are shown in Fig. 9. While both models are able to detect the straight “muon tracks,” the **Cosmic-CoNN** model is better at detecting the complete “worm-shaped” CRs that frequently appear in the *GMOS-N/S* images. The visible discrepancy from **deepCR**’s prediction verified our concern over the batch normalization’s dependency on training data’s statistics (discussed in §3.3). The instrument-specific model produced by the **deepCR** framework per-

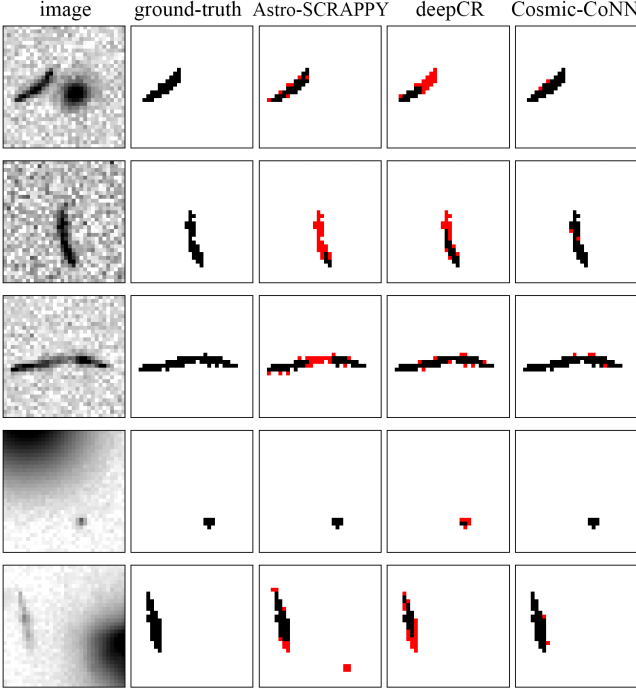


Figure 8. Detection discrepancy on *LCO* imaging data. Incorrect or missing CR pixels are marked in red. **Cosmic-CoNN** detects more peripheral CR pixels than other methods. Comparing to **deepCR**, which was also trained on *LCO* CR dataset, **Cosmic-CoNN**’s prediction is more faithful to ground-truth labels.

forms much better on the test portion of the *LCO* training dataset but lacks the generality for new instruments that are not included in the training data.

The **Cosmic-CoNN** model’s consistent performance on data from other CCD imagers also shows the large, diverse *LCO* CR dataset produces rich cosmic-ray feature coverage that could be effectively generalized to other ground-based instruments. Fig. 11 (top row) shows the detection result of a heavily CR-contaminated image.

4.3. Space-based imaging data

We trained a **Cosmic-CoNN** model with the *HST ACS/WFC* F606W dataset consisting of extragalactic field, globular cluster, and resolved galaxy observations that [Zhang & Bloom \(2020\)](#) released with **deepCR**. Unlike the *LCO* CR dataset which released full-size images in FITS format, images in this dataset are stored as 256² pixel stamps in Numpy arrays, so we were not able to test the effect of larger sampling stamp size (discussed in §3.2) on this dataset.

Given the identical dataset, the model trained with the **Cosmic-CoNN** framework still manages to improve the detection performance in all three types of space-based observations. Particularly in resolved galaxy observations, the TPR improved by over 8% at 0.01% FPR

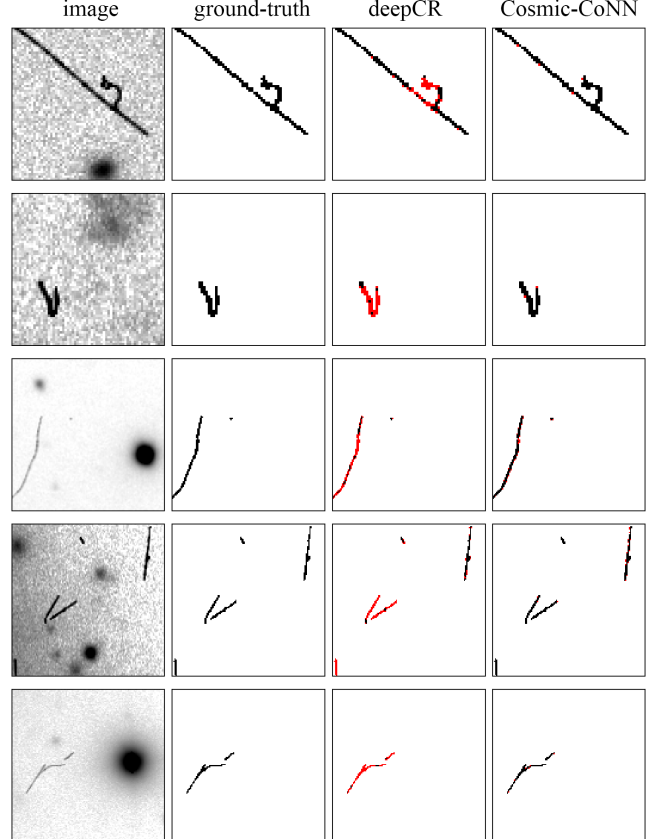


Figure 9. Detection discrepancy on *GMOS-N/S* data. Incorrect or missing CR pixels are marked in red. **Cosmic-CoNN** is able to detect complete CRs of arbitrary shapes, while **deepCR** tends to miss the “worm-shaped” CRs.

comparing to the **deepCR** model (version 0.1.5), as shown in Fig. 10 and Table 2. Optimized for ground-based imaging data, **Cosmic-CoNN** trained effortlessly on the *HST ACS/WFC* data with better performance, which again demonstrates the framework’s broad applicability.

4.4. Spectroscopic data

Finally, we expand the **Cosmic-CoNN** framework to detecting CRs in single-exposure spectroscopic images, a task that has remained challenging for conventional methods. [Bai et al. \(2017\)](#) was able to detect as many as 80% of the CRs in single-exposure, multi-fiber spectral images. Based on two-dimensional profile fitting of the spectral aperture, their method takes about 20 minutes to process a 4K × 4K pixel image. **Cosmic-CoNN** detects nearly all CRs in about 25 seconds on CPU and less than 5 seconds with GPU acceleration.

To prepare the data for deep-learning training, we modified our custom CR-labeling pipeline (Appendix A) and produced a dataset of over 1,500 images using repeated observations from the four instruments of *LCO*’s *Network of Robotic Echelle Spectrographs* (*NRES*) lo-

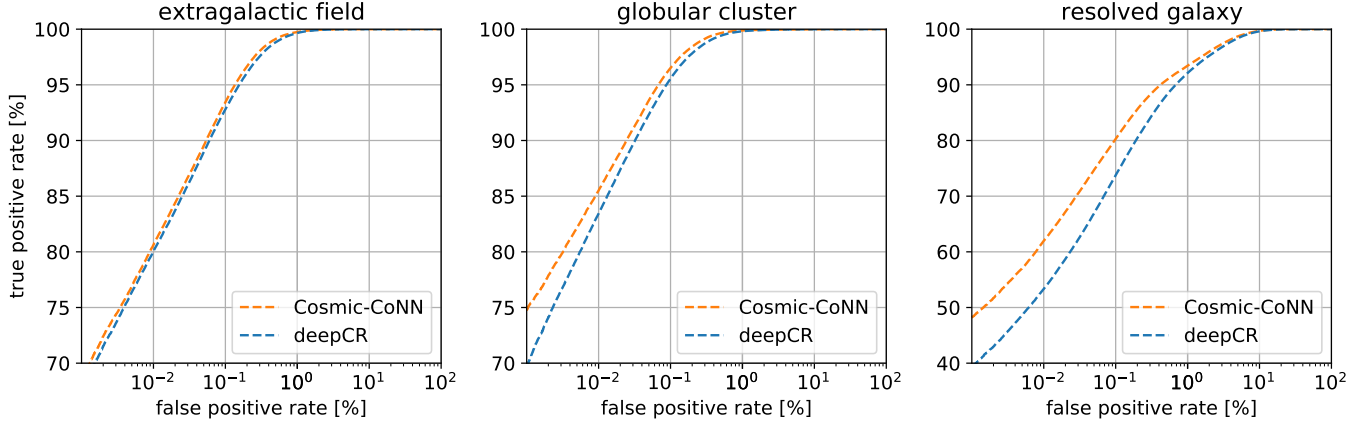


Figure 10. Evaluating models on *HST ACS/WFC* F606W data with ROC curves. **Cosmic-CoNN** has better performance in all three types of observations with over 8% improvement in TPR at 0.01% FPR in resolved galaxy. It shows our improvements designed for ground-based imaging data also applies to training better CR detection models for space-based images.

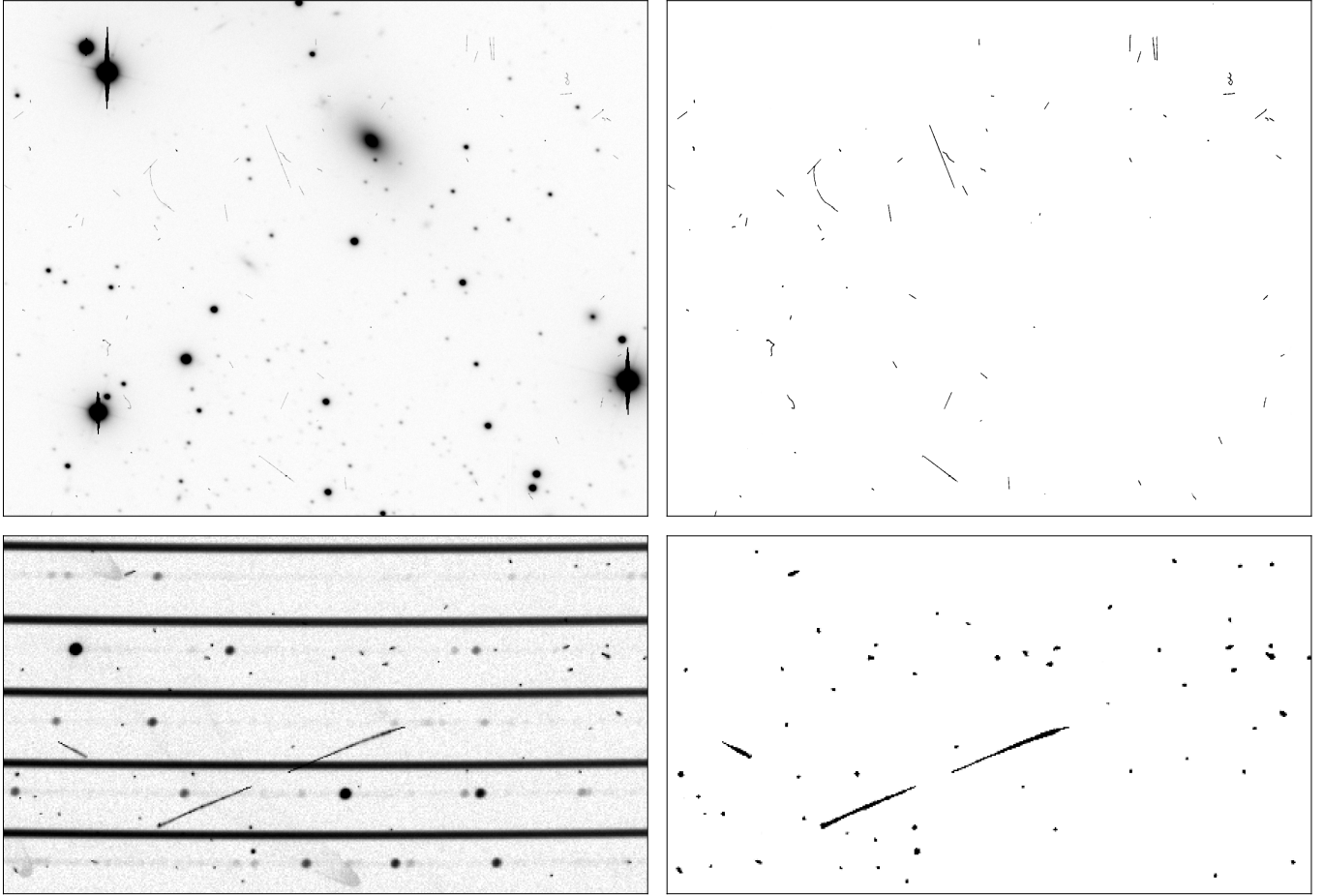


Figure 11. Visual inspection of **Cosmic-CoNN** CR detection results. (Top row) Detecting CRs in a Gemini GMOS-N 1×1 binning image with our generic ground-imaging model. The model was trained entirely on LCO data yet all visible CRs in the image stamp are correctly detected regardless of their shapes or sizes. (Bottom row) **Cosmic-CoNN** NRES model detects CRs over the spectrum robustly on a *LCO NRES* spectroscopic image. The horizontal bands in the left image are the spectroscopic orders, which are left out of the CR mask.

cated around the world. We randomly sampled and re-

served 20% of the data as the test set and used the rest for training and validation.

Cosmic-CoNN reaches 97.40% TPR at 0.01% FPR with a precision of 94.4% at 95% recall, as presented in Table 2. Considering the high CR rates in spectroscopic images because of the 15 minutes or longer exposure time, the NRES model in fact demonstrates exceptional performance. A detection result example is shown in Fig. 11 (bottom row). We consider these results preliminary because the focus of this paper is on a generic ground-based imaging model and we will conduct thorough comparison with other methods in a future work. Nevertheless, the versatility of **Cosmic-CoNN** framework potentially paves a way for solving the CR detection problem in the accuracy-demanding spectroscopic data.

5. TOOLKIT

We have built a suite of tools to democratize deep-learning models in order to make automatic, robust, and rapid CR detection widely accessible to astronomers. The toolkit includes console commands for batch processing FITS files, a web-based app providing CR mask preview and editing capabilities, and Python APIs to integrate **Cosmic-CoNN** models into other data workflows.

The Python toolkit package is released on PyPI. We host the open-source **Cosmic-CoNN** framework on GitHub <https://github.com/cy-xu/cosmic-conn> with complete documentation including toolkit manual, developer instructions on using the LCO CR dataset and training new models. We also released the LCO CR dataset and the code used to generate the results to facilitate reproducibility.

Console commands are the most convenient way to perform batch CR detection on FITS files directly, e.g.,
`$ cosmic-conn -i input -m ground_imaging`
utilizes the generic `ground_imaging` model and the user can replace the argument with `NRES` or `HST_ACS_WFC` for CR detection in other types of data. The result is attached as a FITS extension. In terms of speed, **Cosmic-CoNN** provides more accurate prediction than conventional methods in comparable time on the CPU. Processing a $2K \times 2K$ pixels image takes ~ 7.5 s on a AMD Ryzen 9 5900HS laptop processor. With GPU-acceleration, it takes only ~ 0.8 s on a high-end Nvidia Tesla V100 GPU, and ~ 1.2 s on an entry-level Nvidia GTX 1650 laptop GPU.

The `$ cosmic-conn -a` command starts an interactive CR detector in the browser, as shown in Fig. 12. We adopt the interface layout and controls from the SAOImageDS9 (Joye & Mandel 2003). In addition, we provide an array of CR thumbnails for quick navigation and the ability to edit CR masks in real time. The JavaScript-backed web app provides necessary tools for users to fine-tune the appropriate post-processing

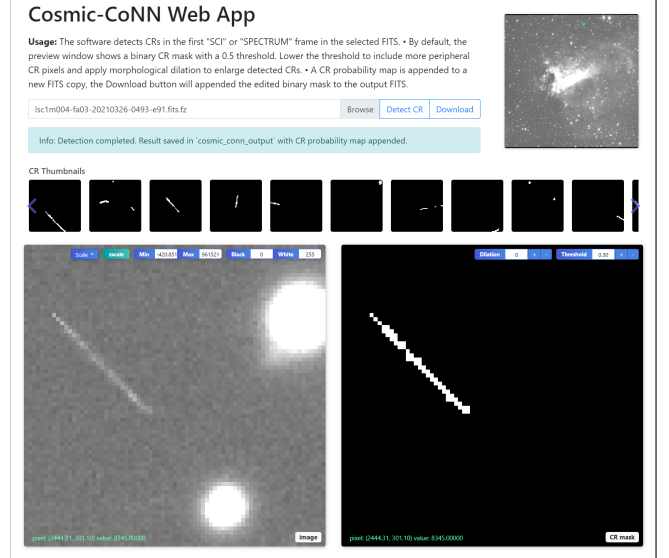


Figure 12. The web app provides synchronized previews of the image and the detection result. An array of CR thumbnails allow users to quickly move the preview windows to the largest CRs for close inspection. This tool is especially useful to help users find the suitable threshold to use in their own data reduction pipeline. Users could manually adjust the threshold on the predicted probability map or apply morphological dilation in real-time to acquire the desirable binary CR mask.

parameters for different instruments. The preview window supports various scaling methods like the `zscale` for better visualization.

Finally, it is also easy to import the `Cosmic-CoNN` as a Python package. Let `image` be a two-dimensional `float32` Numpy array:

```
from cosmic_conn import init_model
# initialize the generic ground-imaging model
cr_model, opt = init_model("ground_imaging")
# the model outputs a CR probability map
cr_prob = cr_model.detect_cr(image)
# convert to a Boolean mask with a 0.5 threshold
cr_mask = cr_prob > 0.5
```

This allows other facilities to integrate rapid CR detection into their data reduction pipeline. The framework checks if the host machine supports GPU-acceleration and prioritizes computation on GPU. Then it optimizes the detection strategy (full image or slice-and-stitch using smaller stamps) based on available memory without human intervention.

We are planning to deploy the web app on the cloud to provide GPU-accelerated CR detection as a free service. This will allow users to upload their failure cases to us to expand the training set and improve the model. In the current release, the web app is a local instance which does not collect or upload any user information.

6. CONCLUSION

In this work, we presented an end-to-end solution to help tackle the CR detection problem in astronomical images. The large, diverse ground-based cosmic ray dataset produces rich feature coverage, allowing deep-learning models to achieve state-of-the-art CR detection on single-exposure images from Las Cumbres Observatory. The `Cosmic-CoNN` deep-learning framework trained generic CR detection models that maintain very high performance on unseen instruments. Extensive evaluation showed the framework's broad applicability in ground- and space-based imaging data, as well as spectroscopic data. Finally, we released a toolkit to make the deep-learning CR detection easily accessible to astronomers.

Using the generic `Cosmic-CoNN` model as a pre-trained initialization, other facilities could fine-tune a model optimized for their own CCD imager with a lot less data. The LCO CR dataset also lays the foundation for a potential universal solution. By expanding our dataset with more instruments from other facilities, we are confident to see an universal CR detection model that achieves better performance on unseen ground-based instruments without further training.

The `Cosmic-CoNN` framework and the toolkit will be a valuable resource for the community to develop future deep-learning methods for source extraction, satellite detection, near-Earth objects detection, and more. These topics are not the focus of this paper but our improvements to the neural network made `Cosmic-CoNN` a suitable deep-learning architecture for these tasks, as we have seen in some preliminary experiments.

With the current `Cosmic-CoNN` model rejecting CRs that could be falsely recognized as astronomical sources, we could better profile the point spread functions in order to address the $\sim 1.21\%$ excluded CR pixels in the next release of our dataset. We expect to see further improvement in the `Cosmic-CoNN` model.

As large surveys like the *Vera Rubin Observatory's Legacy Survey of Space and Time (LSST)* (Ivezić et al. 2019) go online, we will see an explosion of new data that requires automatic, robust, and rapid CR detection. With GPU-acceleration, deep-learning methods like `Cosmic-CoNN` will likely be the solution for future data reduction pipelines that is needed to process the over 100 terabytes of data produced each night from *LSST* and many follow-up facilities.

ACKNOWLEDGMENTS

We thank Yuxiang Wang, Keming Zhang, Jiaxiang Jiang, Chris Hellmuth, Jennifer Jacobs, and Tobias Höllerer for their discussion and feedback on this work. We thank Simon Conseil and the DRAGONS software (Labrie et al. 2019) support team for their help in producing the *Gemini GMOS* evaluation dataset.

This work makes use of observations from the *Las Cumbres Observatory* global telescope network (Brown et al. 2013). This work is also based on observations obtained at the international Gemini Observatory, a program of NSF's NOIRLab, which is managed by the Association of Universities for Research in Astronomy (AURA) under a cooperative agreement with the National Science Foundation on behalf of the Gemini Observatory partnership: the National Science Foundation (United States), National Research Council (Canada), Agencia Nacional de Investigación y Desarrollo (Chile), Ministerio de Ciencia, Tecnología e Innovación (Argentina), Ministério da Ciência, Tecnologia, Inovações e Comunicações (Brazil), and Korea Astronomy and Space Science Institute (Republic of Korea).

Use was made of computational facilities purchased with funds from the National Science Foundation (OAC-1925717) and administered by the Center for Scientific Computing (CSC). The CSC is supported by the California NanoSystems Institute and the Materials Research Science and Engineering Center (MRSEC; NSF DMR 1720256) at UC Santa Barbara. This work was also partially funded by National Science Foundation grants IIS-1619376 and IIS-1911230.

Facilities: *LCOGT*, *HST(ACS/WFC)*, *Gemini:Gillett*, *Gemini:South*

Software: `Astropy` (Astropy Collaboration et al. 2013, 2018), `Astro-SCRAPPY` (McCully et al. 2018), `DRAGONS` (Labrie et al. 2019), `reproject` (Robitaille et al. 2020), `Matplotlib` (Hunter 2007), `NumPy` (Harris et al. 2020), `scikit-image` (van der Walt et al. 2014), `SExtractor` (Bertin & Arnouts 1996), `PyTorch` (Paszke et al. 2019)

APPENDIX

A. CR LABELING PIPELINE

The ground-truth CR-labeling pipeline starts with searching for successive exposures of the same field. We acquire the publicly available scientific observations from *LCO*'s Science Archive¹ and filter the number of visits users requested (more than three but no more than twelve). It is unlikely a cosmic ray will hit the same pixel location twice, so every three consecutive exposures are saved as a sequence into a multi-extension FITS file for alignment and CR labeling, while maintaining all the header information for future community research. For higher signal-to-noise ratio and higher CR rates, we only used images with an exposure time of 100 seconds or longer. We further constrained the consecutive images to be taken within the same schedule molecule, the minimal *LCO* scheduler unit. Images from the same molecule ensure intervals between exposures are minutes or less, which minimize the variations in seeing conditions and point spread function (PSF). We reject a sequence whose background varies over $\sigma > 5$ between frames, as they are not stable enough to robustly identify cosmic rays.

We then reproject to align each frame in the sequence with `astropy/reproject` (Robitaille et al. 2019) using nearest-neighbor interpolation to ensure CRs are not distorted during re-sampling. Fig. 1 shows an image stamp from an aligned sequence. *LCO*'s BANZAI (McCully et al. 2018) data reduction pipeline have bias and dark frame subtracted to remove instrument signature, allowing us to use one CR-labeling pipeline across all *LCO* instruments. Let I be an image in the sequence then I 's noise uncertainty σ_I is simplified to:

$$\sigma_I = \sqrt{|I| + N_R^2 + N_S} \quad (\text{A1})$$

where N_R is the CCD read noise, N_S is the sky background noise, which corrects for the background variation between exposures. We then approximate the median frame uncertainty Σ by performing median filtering at each pixel location across the uncertainties from the three frames I_1 , I_2 , and I_3 in order to reject the variance from the CR pixels:

$$\Sigma = \frac{\text{Median}(\sigma_{I_1}, \sigma_{I_2}, \sigma_{I_3})}{\sqrt{3}}. \quad (\text{A2})$$

We update each frame I with sky subtraction $I := I - \text{Median}(I)$ before calculating the median frame M_I . We then define a deviation score that calculates how much each frame deviates from the median frame represented in Gaussian distribution:

$$\text{Deviation score} = \frac{I - M_I}{\sqrt{(\sigma_I)^2 + \Sigma^2}}. \quad (\text{A3})$$

Pixel locations with a deviation score > 5.0 are identified as bright CR pixels and labeled in a preliminary outlier mask. A morphological dilation of five pixels is applied to the outlier mask, and we use a lower threshold of > 2.5 to include the dimmer peripheral pixels around the CRs.

A key step to acquire the final CR mask is to remove false-positive outliers caused by PSF wings and isolated hot pixels. We perform source extraction with SEP (Barbary 2016) on the CR-free median frame to acquire a robust source catalog. We then perform windowed background estimation to include the astrophysical source pixels in an ignore mask to reject false-positive outlier from PSF wings (Howell 2006).

BANZAI provided a mask for permanent dead CCD pixels but we also noticed a very small fraction of remaining standalone hot pixels that are more likely to be Poisson noise or persistent pixels due to over saturation in previous exposures. Thus our last step is to reject isolated (single) hot pixel events to acquire the final CR mask. Different types of artifacts and rejected pixels, including 100 pixels ignored around CCD boundaries are coded and included in the ignore mask. Instruction on using the data pipeline, the LCO CR dataset, and the ignore mask coding rules can be found in the documentation <https://github.com/cy-xu/cosmic-conn>.

¹ <https://archive.lco.global/>

B. ABLATION STUDY

An ablation study helps us understand how a building block or a design choice affects the overall performance in a machine learning system. It removes or replaces a single component in a controlled experiment to understand its causality. We evaluate the three major deep-learning improvements discussed in Sec. 3 and present the ablation study quantitative results here. Each variant model in Table. 3 replaces a single component in the baseline **Cosmic-CoNN** model while holding other variables constant. We gauge the training efficiency by the number of training epochs a model takes to reach a Dice score > 0.85 (Sørensen 1948). Less epochs means a less convoluted convergence path, as we discussed in §3.1. Precision on *LCO* and *Gemini* data are measured at 95% recall, corresponding to a model’s performance at epoch 5000 shown in Fig. 5, higher is better.

Table 3. **Cosmic-CoNN** ablation study on *LCO* and *Gemini* imaging data. Each variant model suffers certain loss while the **Cosmic-CoNN** model, which benefits from the joint effects of the novel median-weighted loss, the larger 1024^2 pixels sampling stamp size, and group normalization (GN) performs the best in both training efficiency and generality. **Cosmic-CoNN** BN has a similar performance on *LCO* data but it does not generalize well to *Gemini* data.

Method	Dice score > 0.85 (epochs)	LCO Precision	Gemini 1 \times 1 Precision	Gemini 2 \times 2 Precision
Cosmic-CoNN (baseline)	170	94.47%	88.56%	94.57%
Cosmic-CoNN BN	640	94.08%	80.79%	82.6%
Cosmic-CoNN BCE	300	93.52%	82.72%	93.36%
Cosmic-CoNN 256 ²	800	92.52%	76.65%	90.18%

C. TRAINING DETAILS

We implement the **Cosmic-CoNN** framework in PyTorch 1.6.0 (Paszke et al. 2019) with Adam optimizer (Kingma & Ba 2014). Models for the same type of observation are trained with identical data, random seed, and hardware. We use the Nvidia Tesla v100 32GB GPU for training. The large GPU memory allows us to maximize the batch size n in each iteration. All training settings are identical unless it is clearly specified for a variant model. Scripts to reproduce our experiments are included in the source code.

For LCO imaging data, we randomly sampled and withheld 20% of the training set for validation. An initial learning rate of 0.001 was used for all models. During training, we monitor the validation loss for each model and manually decay the learning rate by 0.1 when the loss plateaus. Models using group normalization adopt a fixed `group=8` for all feature layers. For the median-weighted loss we linearly scale the lower bound α from 0 to 1 over 100 epochs. We re-implemented `deepCR` with identical network and adopted the two-phase training that Zhang & Bloom (2020) used to train `deepCR` models. The **Cosmic-CoNN** batch normalization (BN) variant model also adopted the two-phase training. In order to make fair comparison, all **Cosmic-CoNN** and `deepCR` models were carefully tuned, the best models were used for evaluation.

The **Cosmic-CoNN** model and its BN, BCE variants adopt 1024^2 pixels sampling stamp size with a batch size $n = 10$. The `deepCR` and the **Cosmic-CoNN** 256² variant adopt 256^2 pixels stamp size with $n = 160$. For a dataset of N samples, models trained with batch size $n = 10$ updates $\lfloor \frac{N}{10} \rfloor$ times in an epoch but models trained with $n = 160$ only update $\lfloor \frac{N}{160} \rfloor$ times, which leads to unfair comparisons on training efficiency. We addressed this issue by sampling a subset of $\lfloor \frac{N}{16} \rfloor$ samples as an epoch for models with batch size $n = 10$.

For *HST ACS/WFC* imaging data, the **Cosmic-CoNN** model is trained on identical data as `deepCR` (Zhang & Bloom 2020) but with a new PyTorch data loader that added random rotation and mirroring while sampling images. The larger GPU memory allowed us to use 256^2 pixels sampling stamp size with $n = 160$.

For *LCO NRES* spectroscopic data, the neural network is identical to the **Cosmic-CoNN** ground-imaging model. We used a stamp size of 1024^2 pixels with $n = 8$, an initial learning rate 0.0001, and manually monitor and decay the learning rate.

REFERENCES

Astropy Collaboration, Robitaille, T. P., Tollerud, E. J., et al. 2013, *A&A*, 558, A33, doi: [10.1051/0004-6361/201322068](https://doi.org/10.1051/0004-6361/201322068)

Astropy Collaboration, Price-Whelan, A. M., Sipőcz, B. M., et al. 2018, *AJ*, 156, 123, doi: [10.3847/1538-3881/aabc4f](https://doi.org/10.3847/1538-3881/aabc4f)

Bai, Z., Zhang, H., Yuan, H., et al. 2017, *PASP*, 129, 024004, doi: [10.1088/1538-3873/129/972/024004](https://doi.org/10.1088/1538-3873/129/972/024004)

Barbary, K. 2016, *Journal of Open Source Software*, 1, 58, doi: [10.21105/joss.00058](https://doi.org/10.21105/joss.00058)

Baron, D. 2019, arXiv e-prints, arXiv:1904.07248. <https://arxiv.org/abs/1904.07248>

Bertin, E., & Arnouts, S. 1996, *A&AS*, 117, 393, doi: [10.1051/aas:1996164](https://doi.org/10.1051/aas:1996164)

Bottou, L., Curtis, F. E., & Nocedal, J. 2016, arXiv e-prints, arXiv:1606.04838. <https://arxiv.org/abs/1606.04838>

Brown, T. M., Baliber, N., Bianco, F. B., et al. 2013, *Publications of the Astronomical Society of the Pacific*, 125, 1031, doi: [10.1086/673168](https://doi.org/10.1086/673168)

Buda, M., Maki, A., & Mazurowski, M. A. 2018, *Neural Networks*, 106, 249, doi: <https://doi.org/10.1016/j.neunet.2018.07.011>

Chen, J. S., Huertas, A., & Medioni, G. 1987, *IEEE Transactions on Pattern Analysis and Machine Intelligence*, PAMI-9, 584, doi: [10.1109/TPAMI.1987.4767946](https://doi.org/10.1109/TPAMI.1987.4767946)

Desai, S., Mohr, J. J., Bertin, E., Kümmel, M., & Wetzstein, M. 2016, *Astronomy and Computing*, 16, 67, doi: [10.1016/j.ascom.2016.04.002](https://doi.org/10.1016/j.ascom.2016.04.002)

Farage, C. L., & Pimbblet, K. A. 2005, *PASA*, 22, 249, doi: [10.1071/AS05012](https://doi.org/10.1071/AS05012)

Fawcett, T. 2006, *Pattern Recognit. Lett.*, 27, 861, doi: [10.1016/j.patrec.2005.10.010](https://doi.org/10.1016/j.patrec.2005.10.010)

Freudling, W. 1995, *PASP*, 107, 85, doi: [10.1086/133519](https://doi.org/10.1086/133519)

Fruchter, A. S., & Hook, R. N. 2002, *PASP*, 114, 144, doi: [10.1086/338393](https://doi.org/10.1086/338393)

Gillett, F. C., Mountain, M., Kurz, R., et al. 1996, in *Revista Mexicana de Astronomia y Astrofisica Conference Series*, Vol. 4, *Revista Mexicana de Astronomia y Astrofisica Conference Series*, ed. E. Falco, J. A. Fernandez, & R. F. Ferrero, 75

Harris, C. R., Millman, K. J., van der Walt, S. J., et al. 2020, *Nature*, 585, 357, doi: [10.1038/s41586-020-2649-2](https://doi.org/10.1038/s41586-020-2649-2)

Hiramatsu, D., Howell, D. A., Van Dyk, S. D., et al. 2020, arXiv e-prints, arXiv:2011.02176. <https://arxiv.org/abs/2011.02176>

Howell, S. B. 2006, *Photometry and astrometry*, 2nd edn., Cambridge Observing Handbooks for Research Astronomers (Cambridge University Press), 102134, doi: [10.1017/CBO9780511807909.007](https://doi.org/10.1017/CBO9780511807909.007)

Hunter, J. D. 2007, *Computing in Science & Engineering*, 9, 90, doi: [10.1109/MCSE.2007.55](https://doi.org/10.1109/MCSE.2007.55)

Ioffe, S., & Szegedy, C. 2015, in *JMLR Workshop and Conference Proceedings*, Vol. 37, *Proceedings of the 32nd International Conference on Machine Learning, ICML 2015*, Lille, France, 6-11 July 2015, ed. F. R. Bach & D. M. Blei (JMLR.org), 448–456. <http://proceedings.mlr.press/v37/ioffe15.html>

Ivezić, Ž., Kahn, S. M., Tyson, J. A., et al. 2019, *ApJ*, 873, 111, doi: [10.3847/1538-4357/ab042c](https://doi.org/10.3847/1538-4357/ab042c)

Joye, W. A., & Mandel, E. 2003, in *Astronomical Society of the Pacific Conference Series*, Vol. 295, *Astronomical Data Analysis Software and Systems XII*, ed. H. E. Payne, R. I. Jedrzejewski, & R. N. Hook, 489

Kingma, D. P., & Ba, J. 2014, arXiv e-prints, arXiv:1412.6980. <https://arxiv.org/abs/1412.6980>

Labrie, K., Anderson, K., Cárdenes, R., Simpson, C., & Turner, J. E. H. 2019, in *Astronomical Society of the Pacific Conference Series*, Vol. 523, *Astronomical Data Analysis Software and Systems XXVII*, ed. P. J. Teuben, M. W. Pound, B. A. Thomas, & E. M. Warner, 321

Little, W. 1974, *Mathematical Biosciences*, 19, 101, doi: [https://doi.org/10.1016/0025-5564\(74\)90031-5](https://doi.org/10.1016/0025-5564(74)90031-5)

Little, W., & Shaw, G. L. 1978, *Mathematical Biosciences*, 39, 281, doi: [https://doi.org/10.1016/0025-5564\(78\)90058-5](https://doi.org/10.1016/0025-5564(78)90058-5)

McCully, C., Volgenau, N. H., Harbeck, D.-R., et al. 2018, in *Society of Photo-Optical Instrumentation Engineers (SPIE) Conference Series*, Vol. 10707, *Software and Cyberinfrastructure for Astronomy V*, ed. J. C. Guzman & J. Ibsen, 107070K, doi: [10.1117/12.2314340](https://doi.org/10.1117/12.2314340)

McCully, C., Crawford, S., Kovacs, G., et al. 2018, *astropy/astroscrappy*: v1.0.5 Zenodo Release, v1.0.5, Zenodo, doi: [10.5281/zenodo.1482019](https://doi.org/10.5281/zenodo.1482019)

Miles, N., Deustua, S. E., Tancredi, G., et al. 2020, arXiv e-prints, arXiv:2006.00909. <https://arxiv.org/abs/2006.00909>

Murtagh, F. D., & Adorf, H. M. 1991, in *European Southern Observatory Conference and Workshop Proceedings*, Vol. 38, *European Southern Observatory Conference and Workshop Proceedings*, 51

Paszke, A., Gross, S., Massa, F., et al. 2019, arXiv e-prints, arXiv:1912.01703. <https://arxiv.org/abs/1912.01703>

Pych, W. 2004, *PASP*, 116, 148, doi: [10.1086/381786](https://doi.org/10.1086/381786)

Rhoads, J. E. 2000, *PASP*, 112, 703, doi: [10.1086/316559](https://doi.org/10.1086/316559)

Robbins, H., & Monro, S. 1951, *The Annals of Mathematical Statistics*, 22, 400 , doi: [10.1214/aoms/1177729586](https://doi.org/10.1214/aoms/1177729586)

Robitaille, T., Deil, C., & Ginsburg, A. 2020, reproject: Python-based astronomical image reprojection. <http://ascl.net/2011.023>

Robitaille, T., Ginsburg, A., & Deil, C. 2019, astropy/reproject. <https://github.com/astropy/reproject>

Ronneberger, O., Fischer, P., & Brox, T. 2015, arXiv e-prints, arXiv:1505.04597. <https://arxiv.org/abs/1505.04597>

Saito, T., & Rehmsmeier, M. 2015, PLoS ONE, 10, e0118432, doi: [10.1371/journal.pone.0118432](https://doi.org/10.1371/journal.pone.0118432)

Salzberg, S., Chandar, R., Ford, H., Murthy, S. K., & White, R. 1995, PASP, 107, 279, doi: [10.1086/133551](https://doi.org/10.1086/133551)

Shamir, L. 2005, *Astronomische Nachrichten*, 326, 428, doi: [10.1002/asna.200510364](https://doi.org/10.1002/asna.200510364)

Sørensen, T. J. 1948, A method of establishing groups of equal amplitude in plant sociology based on similarity of species content and its application to analyses of the vegetation on Danish commons, Vol. 5 (Munksgaard Copenhagen)

Sudre, C. H., Li, W., Vercauteren, T., Ourselin, S., & Cardoso, M. J. 2017, arXiv e-prints, arXiv:1707.03237. <https://arxiv.org/abs/1707.03237>

Summers, C., & Dinneen, M. J. 2019, CoRR, abs/1906.03548. <https://arxiv.org/abs/1906.03548>

van der Walt, S., Schönberger, J. L., Nunez-Iglesias, J., et al. 2014, PeerJ, 2, e453, doi: [10.7717/peerj.453](https://doi.org/10.7717/peerj.453)

van Dokkum, P. G. 2001, PASP, 113, 1420, doi: [10.1086/323894](https://doi.org/10.1086/323894)

Windhorst, R. A., Franklin, B. E., & Neuschaefer, L. W. 1994, PASP, 106, 798, doi: [10.1086/133443](https://doi.org/10.1086/133443)

Wu, Y., & He, K. 2018, CoRR, abs/1803.08494. <https://arxiv.org/abs/1803.08494>

Zhang, C. Y. 1995, in *Astronomical Society of the Pacific Conference Series*, Vol. 77, *Astronomical Data Analysis Software and Systems IV*, ed. R. A. Shaw, H. E. Payne, & J. J. E. Hayes, 514

Zhang, K., & Bloom, J. S. 2020, ApJ, 889, 24, doi: [10.3847/1538-4357/ab3fa6](https://doi.org/10.3847/1538-4357/ab3fa6)